High-Sensitivity Focus-Induced Photoresponse in Amorphous Silicon Photodiodes for Enhanced Three-Dimensional Imaging Sensors

Maurice Müller,[*] Andreas Bablich,[†] Paul Kienitz, Rainer Bornemann, Charles O. Ogolla, Benjamin Butz, and Peter Haring Bolívar
School of Science and Technology, University of Siegen, Hölderlinstr. 3, 57076 Siegen, Germany

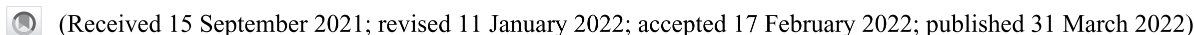
(Received 15 September 2021; revised 11 January 2022; accepted 17 February 2022; published 31 March 2022)

In this work, we report on the bias-tunable and highly sensitive irradiance-dependent focus-induced photoresponse (FIP) in amorphous silicon *p-i-n* diodes for enhanced three-dimensional imaging applications. We identify a nonlinear current breakdown at irradiance down to at least 0.6 μW/mm^2 due to defect-induced electrical field screening, surpassing state-of-the-art device sensitivities by at least a factor of 16 in the visible range. We further demonstrate the tunability of FIP by systematic device and field engineering to enable both precise and long-range high-resolution distance measurements in just one device architecture. We evaluate distance measurements up to at least 15 m and achieve a depth resolution of 2.1 mm at 3.3 m. The reproducible low-temperature (300 °C or lower) plasma-enhanced chemical vapor-deposition technology enables systematic tailoring of the FIP for three-dimensional imaging applications and allows for back-end sensor integration on top of silicon or flexible electronics with fill factors up to 100%.

DOI: 10.1103/PhysRevApplied.17.034075

I. INTRODUCTION

A huge and growing number of applications, such as scene detection for autonomous driving [1], smart manufacturing instrumentation [2], augmented and virtual reality [3] as well as three-dimensional entertainment [4] benefit from simple, precise, fast and high-resolution three-dimensional imaging components. Therefore, a wide range of distance sensors and three-dimensional imaging techniques have been developed in the past. Most common systems are based on the time-of-flight principle, such as silicon- or two-dimensional-material-based photonic mixer devices [5,6] or light detection and ranging concepts [7]. Both techniques rely on high-intensity light sources, complex readout mechanisms, and device architectures. Dynamic vision also requires complex data acquisition and interpretation [8].

Focus-induced photoresponse (FIP) is a promising and sensitive three-dimensional imaging technique exploiting the nonlinear, irradiance-dependent current response in photonic devices [9]. This technique allows for a simple sensor readout enabling high data rates, a scalability with fill factors up to 100%, and precise (micrometer-range) and long-distance measurements with fluences in the visible range of, up to now, at least 10 μW/mm^2 [9]. Exploiting visible light in prospective FIP-based high-performance three-dimensional camera systems potentially enables simple scene detection with environmental light. FIP has been demonstrated in various thin-film devices including PbS photoconductors, organic dye-sensitized solar cells based on mesoporous TiO_2 and spiro-MeOTAD, amorphous solar cells, and organic photodetectors with BDP-OMe:C_{60} containing a significant number of defects within the mobility gap [9–11]. The mechanisms causing a nonlinear photoresponse vary widely and depend on material compositions and device architectures. Besides charge carrier trapping and photoconductivity variations [12,13], local resistivity changes, for example in PbS photoconductors shown in [9], result in a responsivity breakdown. The classical saturation of defect states can lead to an FIP effect with a positive sign (i.e., increasing irradiances lead to higher photocurrents). This effect will hold true for a wide class of disordered or defect-dominated photodetector materials. Since there is only a need for a nonlinear detector output, all formerly presented FIP devices and architectures in general can be used for distance measurements. Therefore, the shape of the nonlinearity and the minimum irradiance define achievable depth resolutions and distances.

Hydrogenated amorphous silicon (*a*-Si:H) has the advantage of scalable fabrication on top of silicon complementary metal oxide semiconductor microchips due to the low deposition temperature utilizing plasma-enhanced chemical vapor deposition (PECVD) [14]. The manufacturing technique also allows the properties of the devices,

[*]maurice.mueller@uni-siegen.de
[†]andreas.bablich@uni-siegen.de

 © 2022 American Physical Society

such as defect densities and their energetic positions [15], to be adjusted precisely and with a high degree of reproducibility. Additionally, the *a*-Si:H technology benefits from long-term device stability compared to dye-sensitized and organic devices [16,17].

In this work, an irradiance-dependent breakdown of the overall current of two fundamentally different *a*-Si:H photodetectors has been systematically investigated and studied. Electro-optical simulations clearly reveal the physical cause of the nonlinear current breakdown and allow us to predict, model, and optimize *a*-Si:H FIP devices. Based on the simulation results, sensor structures with different thicknesses and material properties have been designed and fabricated by varying PECVD process parameters. Irradiance and bias voltage V_{bias} dependencies on FIP detectors have been studied comprehensively to validate functionalities and to assess quantitative performance advantages compared to earlier demonstrations. Finally, distance measurements based on the *z*-scan photoresponse have been modeled to conduct and to quantify the performance for three-dimensional sensing applications.

II. METHODS

Z-scan current measurements were modeled utilizing a Gaussian beam profile as illumination source to define spot dimensions and the resulting photon flux on the device surface by keeping the total light power constant. The photon flux serves as an input for electro-optical simulations using AFORS-HET [18]. The simulations take illuminated and nonilluminated areas on the sensor surface into account. Detailed information about electro-optical simulation procedures is given in the Supplemental Material [33].

a-Si:H thin-films were deposited by PECVD at temperatures below 300 °C in a hot-wall MVSystems multichamber deposition system on precleaned glass substrates. Transparent and conductive oxide front and back contacts were sputtered in a radio frequency hot-wall sputtering reactor at 13.56 MHz. The devices were structured using standard UV lithography, mounted in dual-inline chip carriers and contacted via wedge bonding [cf. Fig. 1(a)]. Further fabrication details are given in the Supplemental Material [33] as well as in Ref. [19].

Growth rates and thin-film thicknesses of amorphous silicon and contact layers were characterized by cross-sectional backscatter scanning electron microscopy (SEM) imaging using an FEI Quanta 250 environmental scanning electron microscope (ESEM, beam energy 20 keV, 50 Pa nitrogen atmosphere for charge compensation) [cf. Fig. 1(b)]. The clean cross-section was prepared by cleaving after 2 min cooling in liquid nitrogen. Total device thicknesses were thoroughly validated by a Bruker Dektak XT profilometer.

Z-scan measurements were performed utilizing a confocal laser scanning microscope (Nikon TE300 and Nikon PCM2000, numerical aperture NA = 0.6) in combination with a 488-nm laser (JDS Uniphase, 10 mW CW) in front of the scanning unit. To achieve precise *z*-positioning, the microscope lens was moved relative to the detector. Detector currents were digitized using a FEMTO DLPCA-200 *I*-*V* converter in conjunction with an 8-bit video framegrabber as the digitizing unit of the Nikon PCM2000. The total optical power on the detectors was adjusted by optical filters and determined by a crystalline silicon detector

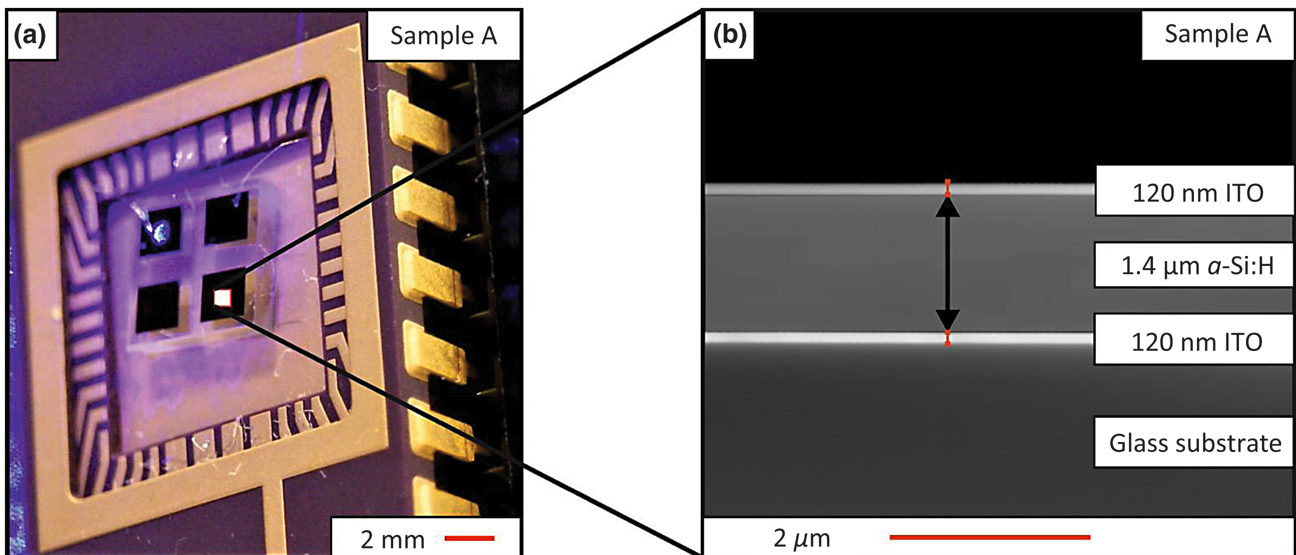

FIG. 1. (a) Photograph and (b) geometrically corrected cross-sectional ESEM micrograph (after FIB cross-sectioning) of an *a*-Si:H *p*-*i*-*n* FIP photodetector, here shown for sample A with indium tin oxide (ITO) contacts.

(Hamamatsu S1337-33BQ). Bias voltages were provided by the *I*-*V* converter.

III. RESULTS AND DISCUSSION

The *z*-scan technique is a well-established method to quantify and characterize optical nonlinearities in solids, liquids, or solutions [20], by adjusting the distance *z* of the focal plane of a laser and the sample surface and measuring optical transmission changes. In this work, we adapt this approach and quantify the total current response of *a*-Si:H *p*-*i*-*n*-photodiodes for different irradiances by keeping the total light power constant and varying the photodetector position with respect to the focus.

In the past, it was observed that the responsivity of *a*-Si:H solar cells with a thickness of 500 nm *increases* near the focal plane [9]. Such a nonlinear responsivity enhancement coincides with the results presented in [21], where a degradation in transmission and an increase in absorption of bare *a*-Si:H thin films near the focal plane has been reported. Such observations could be attributed to a defect saturation associated with an increase in conductivity and photoresponsivity at higher irradiances. However, the simulation and measurement results presented in this work extend earlier observations and reveal that electric field screening due to charge carrier trapping in defect states is the dominant origin in *a*-Si:H *p*-*i*-*n* diodes thicker than 500 nm for a nonlinear FIP response, which manifests itself as a nonlinear *decrease* of the total device current at a photon flux around 10^{15} photons/cm^{2}s.

A. *z*-scan photoresponse simulations

An electro-optical model of the *z*-scan photoresponse was developed to conduct simulations by adapting the AFORS-HET software [18]. The simulations were executed for two different *a*-Si:H *p*-*i*-*n* diode structures (samples A and B) by varying the photon flux as a result of the *z*-scan displacement. All simulations were conducted at four different photon fluxes (cf. Table I) and a fixed bias voltage of 0 V to eliminate noninternal influences on the electric field.

The samples primarily differ in their thicknesses and defect densities of the intrinsic (*i*) layer and were optimized towards a broad (sample A) and steep, intensified bias-tunable FIP (sample B). In the developed simulation setup, photon fluxes of a 488-nm monochromatic light source were converted to the appropriate *z*-positions. Further details on the electro-optical simulation routine and the sample structures are given in the Supplemental Material [33].

TABLE I. Simulated illumination scenarios including the photon flux as simulation input, corresponding irradiance and *z*-position of the detector.

Illumination state	Photon flux, ϕ (photons/cm^{2}s)		Irradiance (W/m^2)	*z*-position (nm)
Dark	ϕ_0	0	0	∞
Low	ϕ_1	10^{15}	4.07	26
Moderate	ϕ_2	10^{17}	407	2.6
Intense	ϕ_3	10^{19}	40 706	0.26

Among other internal statistics and parameters, the simulation software provides information about the electric field distribution, local charge carrier densities of free and trapped charges Q_{tr} (tr stands for trapped), and the energy band diagram including the quasi-Fermi levels of holes E_{fp} and electrons E_{fn}, respectively. Due to the large amount of defects within the mobility gap, the amount of trapped charges in *a*-Si:H is comparatively high and dominates the total space charge ρ over a wide range of low and moderate illumination intensities [22]. Following Poisson's equation

$$\nabla E = \frac{\rho}{\varepsilon}, \tag{1}$$

the internal electric field E increases with a net hole-trapping space charge ρ_+ and decreases with a net electron-trapping space charge ρ_-. Here, ε is the permittivity of *a*-Si:H.

In order to further understand the trapping mechanism within the device, the band structure including the quasi-Fermi energies in conjunction with the density-of-state (DOS) distribution across the intrinsic layer were analyzed. The locally occupied states can be described considering the defect concentration distribution $N_{A,D}(E)$ and the Fermi-Dirac occupation function $f_{n,p}(E)$ [23]

$$n_t = \int_{E_V}^{E_C} N_A(E) \cdot f_n(E) dE \quad \text{and}$$
$$p_t = \int_{E_V}^{E_C} N_D(E) \cdot f_p(E) dE. \tag{2}$$

1. Sample A ($l_{i\text{-}a\text{-Si:H}}$:1526 nm)

Figure 2 shows the energy diagrams of sample A across the 1526-nm-thick intrinsic layer for ϕ_0, ϕ_1, and ϕ_2 (a) and for ϕ_0, ϕ_2, and ϕ_3 (b). Figures 2(c) and 2(d) show the corresponding energetic DOS distributions, including the position of the quasi-Fermi energies along the intrinsic layer.

In the dark state, the Fermi energy E_F remains constant and does not split into $E_{\mathrm{fn,n}}$ [cf. Figs. 2(a)–2(c)]. It is important to evaluate the position x within the intrinsic layer of equally trapped electrons and holes in defects, as this position indicates a turning point of the electric field. Physically, this value depends on the energetic position of $E_{\mathrm{fn,n}}$ and the DOS distribution of the material. In the dark state (ϕ_0), this position can be determined to be $x_0 = 780$ nm within the device, obtaining a maximum of the electric field [cf. Fig. 3(c)]. Figures 3(a)

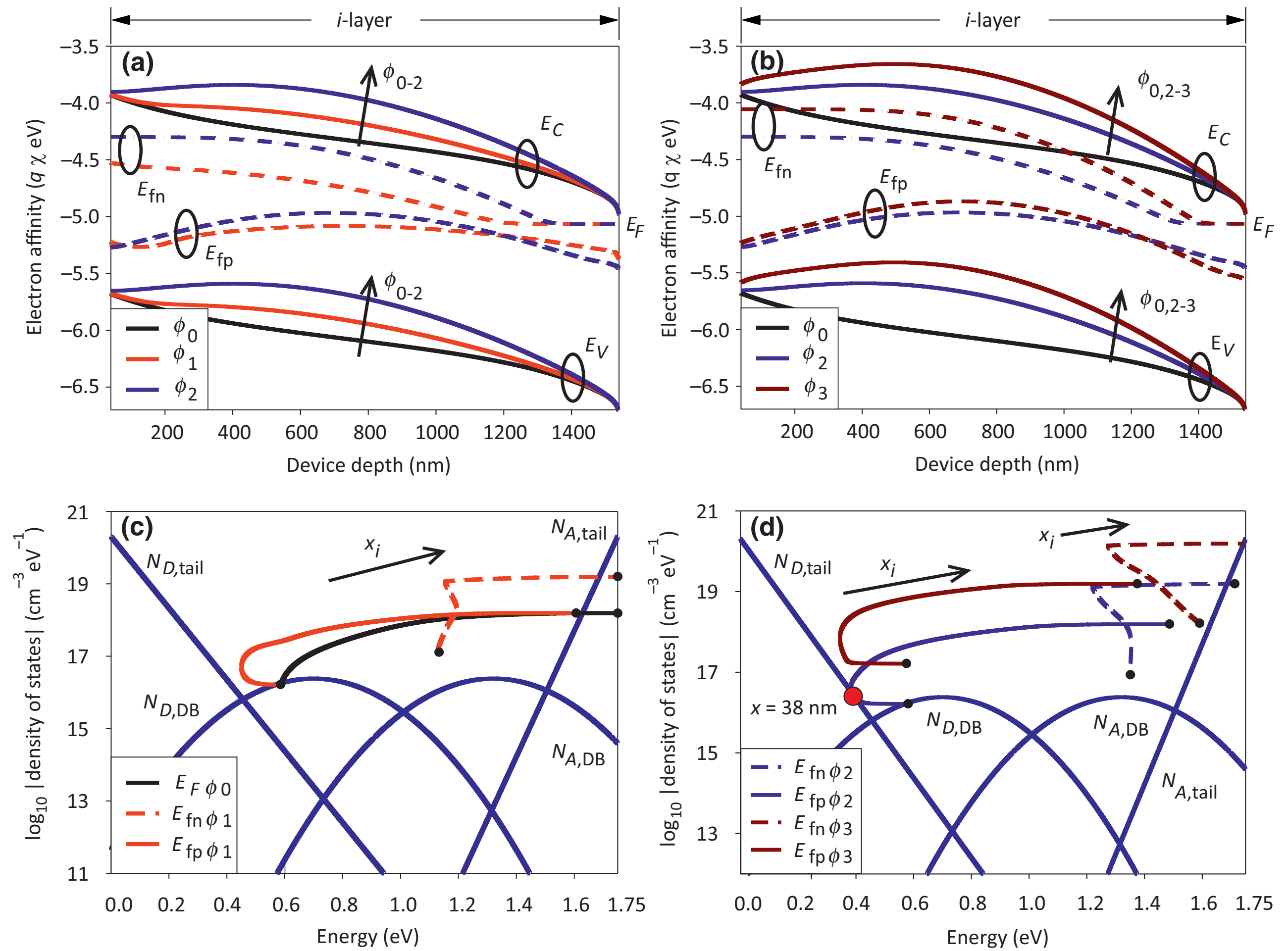

FIG. 2. (a) and (b) Simulated energy band diagrams and [(c) and (d)] density of state distributions within the mobility gap for sample A at varying photon fluxes at 488 nm. (c) and (d) The corresponding quasi-Fermi energies of electrons and holes have been included across the intrinsic layer position x_i to illustrate photo-induced charge-carrier trapping in the tail-state defects $N_{D,\text{tail}}$ and $N_{A,\text{tail}}$ and dangling bond defect states $N_{D,\text{DB}}$ and $N_{A,\text{DB}}$ at different illumination scenarios.

and 3(b) present the concentration of electrons, holes, and net trapped charge carrier density. The total net charge carrier density Q_t which is dominated by the charge trapped in defect states Q_{tr}, changes its type from holes in the front to electrons in the device back at the position x_0 [cf. Fig. 3(a)]. Without illumination, the density of free holes and electrons is comparatively small. The simulated electrical field coincides with Crandall's uniform field theory [24] employing modified boundary conditions.

At higher irradiances, the number of photoinduced charge carriers automatically increases. Therefore, the Fermi level splits into $E_{\text{fn,n}}$ as shown in Fig. 2. The quasi-Fermi energies of electrons and holes do not split symmetrically due to charge carrier separation after generation of an electron-hole pair, taking into account the massively diverging charge carrier mobilities and the donor-acceptor defect distribution characteristics. Close to the *p*-*i* interface at a device depth of $x = 38$ nm, E_{fp} slightly touches the energy level of the valence band tail states $E_{V,\text{tail}}$ [cf. Fig. 2(d)]. Once E_{fp} is energetically located within the valence band tail, a significantly higher amount of net trapped holes locally occurs compared to the dark state. According to Poisson's equation, this automatically leads to a more pronounced field gradient, as seen in Fig. 3(c). By keeping the external bias voltage constant, the field in the back of the intrinsic layer decreases compared to the dark state.

This field deformation increases at higher illumination levels due to a more pronounced asymmetric splitting of $E_{\text{fn,n}}$ as described earlier. Figure 2(d) shows an increased splitting of $E_{\text{fn,n}}$ at higher irradiances ϕ_2, ϕ_3 and reveals the position where E_{fp} penetrates into $E_{V,\text{tail}}$, resulting in a local increase of net trapped holes [cf. Fig. 3(b)]. The majority charge carrier type of the trapping states changes and the electric field obtains a maximum at the position $x_2 = 180$ nm for ϕ_2. For the first time, the internal electric field at the device front changes its sign and becomes positive [cf. Fig. 3(c)]. Such a field reversal is generally known

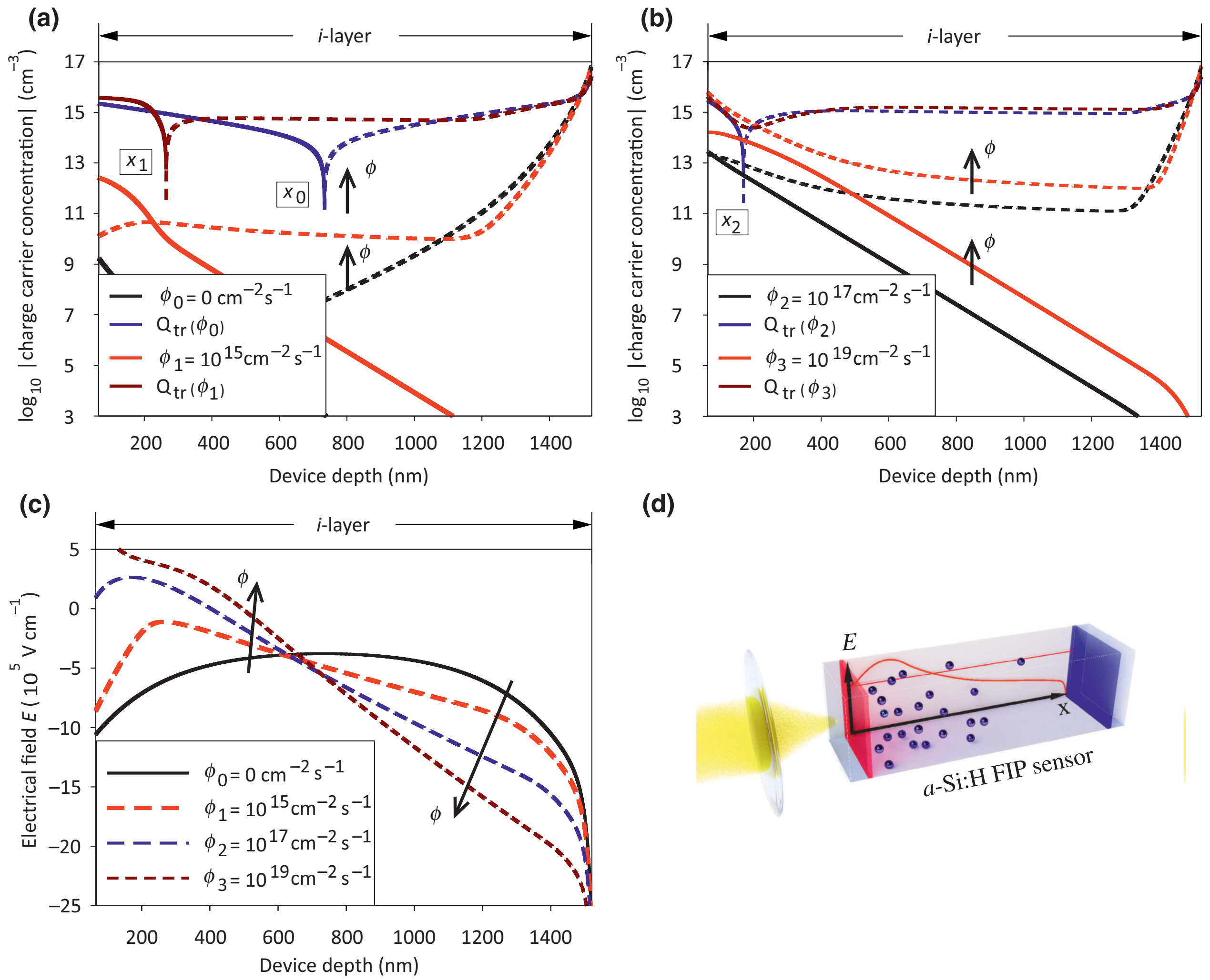

FIG. 3. (a) and (b) Simulated charge carrier concentrations for electrons (dashed lines) and holes (solid lines), (c) electric field distributions as a function of the detector position across the intrinsic layer x_i of sample A for different photon fluxes at 488 nm, and (d) the total electric field screening mechanism due to irradiance induced charge trapping (blue circles).

in the case of applied voltages near the open-circuit voltage of solar cells [25,26] but has not been reported as a result of increasing irradiances at a fixed external bias voltage. The positive field in the device front lifts the valence and conduction band edges in the corresponding area, generating a barrier for charge carrier separation. In result, the collection efficiency and total device current are reduced. For ϕ_2, the position $x_{c,e-} = 400$ nm (here the electric field vanishes completely within the i-layer) determines the maximum achievable charge collection depth for electrons between the position x and the n-type a-Si:H interface. A comparable collection zone for holes expands from the p-type a-Si:H. This statement also holds true for a photon flux of ϕ_3, where the destructive, defect-induced field in the device front dominates the built-in field results in a more pronounced positive electric field in the device front in conjunction with an increase of free electrons [cf. Fig. 3(c)]. As a result, the collection zone for electrons is quenched drastically and the collection zone for holes vanishes completely, so that the overall collection efficiency and the total device current are reduced.

The total mechanism of illumination induces trapped charges in the front of the intrinsic layer, resulting in electric field screening is qualitatively shown in Fig. 3(d).

2. Sample B ($l_{i-a-\mathrm{Si:H}}$:1350 nm)

To further investigate the physical cause of the nonlinear current breakdown in a-Si:H p-i-n photodiodes, irradiance-dependent electro-optical z-scan simulations were conducted for a second device, differing in the thickness of the intrinsic layer (1350 nm) and the defect density inside the intrinsic layer halved compared to sample A.

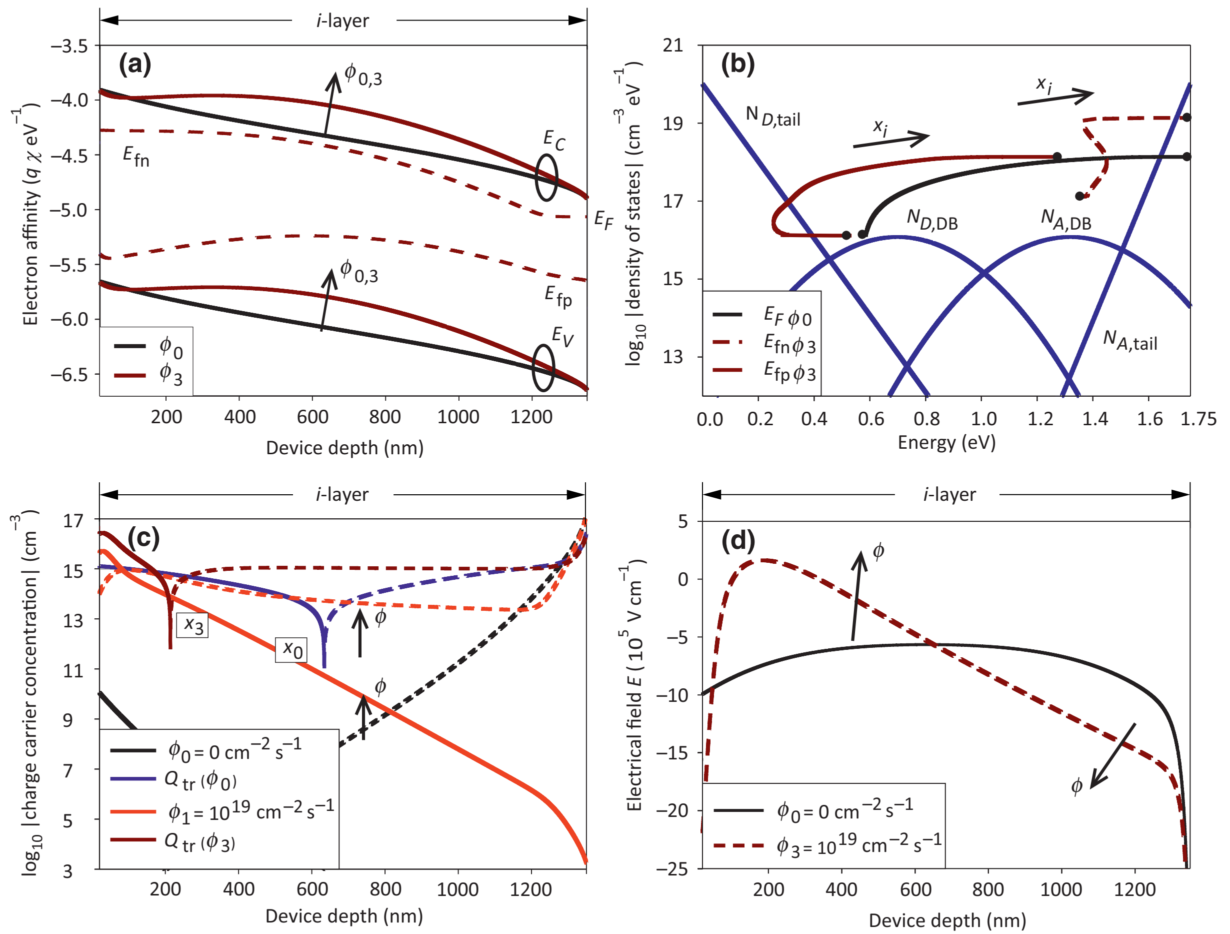

FIG. 4. (a) Simulated energy band diagrams, (b) density of state distributions within the mobility gap including quasi-Fermi energies of electrons and holes, (c) charge carrier concentration for electrons (dashed lines) and holes (solid lines), and (d) electrical field distribution as a function of the detector position across the intrinsic layer x_i of sample B for the dark state $\Phi_0 = 0$ photons/cm^{2}s and a photon flux of $\Phi_3 = 10^{19}$ photons/cm^{2}s corresponding to high irradiance levels at 488 nm.

The simulation results are shown in Fig. 4 for photon fluxes of ϕ_0 and ϕ_3, confirming the mechanisms of the electric field deformation as described earlier for sample A. However, the trap-assisted destructive field screening for sample B has less influence due to the higher absolute built-in field allocated by the thinner intrinsic region and reduced trapping states compared to sample A. For sample B, the electric field remains comparatively stable over a wide range of irradiance levels. A significant influence of the irradiance on the electric field becomes evident at ϕ_3 [cf. Fig. 4(d)]. At ϕ_3, E_{fp} and E_{fn} split asymmetrically and cause a different occupation of defect states across the intrinsic layer. The majority charge carrier type of the trapping states changes and the electric field obtains a maximum at $x_3 = 186$ nm for ϕ_3 compared to the dark state [$x_0 = 634$ nm, cf. Fig. 4(c)] so that the overall collection efficiency and current are reduced. The simulation results reveal that the device current of sample B is much more robust toward irradiance variations at low z-displacements than the current of sample A. In addition, it can clearly be concluded that the nonlinear current breakdown near the focal plane is more pronounced in sample B since the electric field collapse already dominates at lower irradiances in sample A. The simulation results of two *a*-Si:H *p-i-n* photodiodes with different intrinsic layer thicknesses and defect distributions verify that the irradiance-dependent FIP can simply be tuned and tailored by a proper sensor design based on a systematic field and defect engineering.

B. *z*-scan current measurements

Based on the simulation results, *z*-scan measurements have been conducted on the previously discussed *a*-Si:H *p-i-n* detectors. The *z*-scan current measurements in Fig. 5 reveal a sensor- and bias-dependent decrease of the total current near the focal plane at a wavelength of 488 nm and an overall power of 150 μW. The current breakdown for both *a*-Si:H sensor structures coincides with the simulation results presented in the

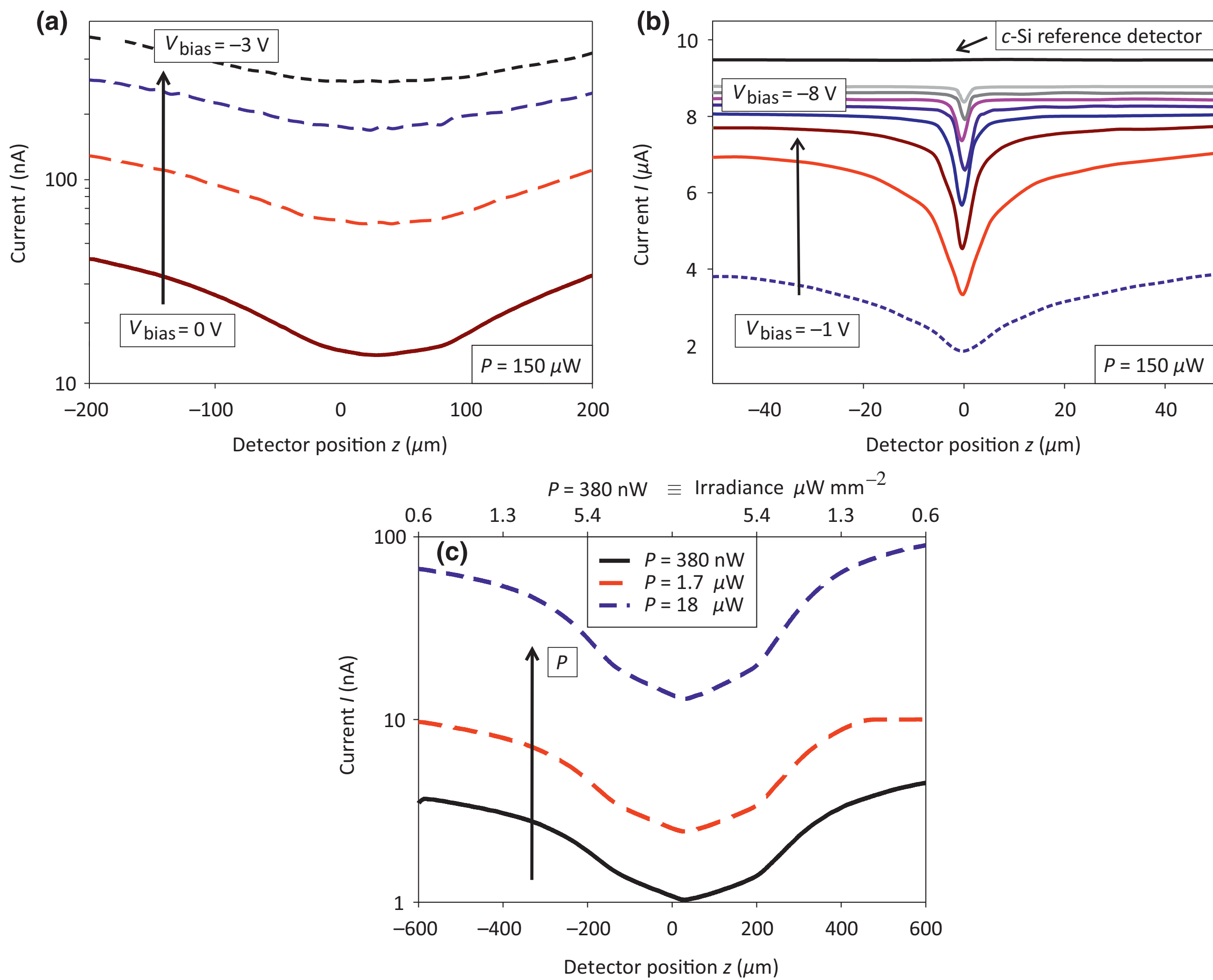

FIG. 5. (a) Bias dependent z-scan measurements of sample A, and (b) sample B for $P = 150\ \mu$W ($\Delta V_{\text{bias}} = 1$ V). Depending on the bias voltage and the sensor architecture, the nonlinear current breakdown can precisely be engineered and adjusted to meet application specific requirements. (c) Intensity dependence of the z-scan measurement of sample A for different light intensities at 488 nm. The current breakdown occurs at an optical power below 380 nW corresponding to intensities $< \mu$W/mm^2 far out of focus.

previous section. As expected, a low-defect monocrystalline silicon reference sensor does not exhibit any irradiance current dependency [cf. Fig. 5(b), black line]. A useful feature of $a-$Si:H photodetectors is that the FIP nonlinearity parameters and response dynamics can be precisely adjusted for application-specific purposes by adjusting material parameters and device architectures such as the i-layer thickness and defect concentration. A further specific advantage of our devices is that characteristics can be controlled by applying an external bias voltage. A bias-dependent FIP has not previously been reported for other FIP detectors [9,10]. Figure 5(a) shows the bias-dependent z-scan measurement results of sample A which has been optimized to obtain a broad FIP as a prerequisite for high-sensitivity long-range distance measurements. In this context, “broad” means an FIP nonlinearity which varies over a wide range of focus displacements. At 0 V bias, the FIP is more pronounced compared to the z-scan response at reverse bias.

Compared to sample A, the bias tunability of the FIP in sample B is much more sensitive and the tailored design enables both precise and mid- and long-range distance measurements utilizing just one sensor architecture. At −3 V bias, sample B exhibits a steep and narrow current breakdown, a desirable feature for high-depth resolution distance measurements [cf. Fig. 7(b)]. Applying a bias of −1 V to sample B also enables measurement at larger distances with the same device due to the broader detector position dependence of the FIP. Increasing the bias voltage to more negative values increases the electrical field across the intrinsic region so that trap-assisted field screening and therefore the FIP is quenched. The field breakdown in both samples

has been engineered to enable high-sensitivity distance measurements at very low irradiance levels. Figure 5(c) reveals that the FIP in sample A occurs at an optical power below 380 nW for 488 nm corresponding to an irradiance down to at least 0.6 μW/mm^2. This surpasses the current sensitivity benchmark for FIP detectors of 10 μW/mm^2 on the detector surface by at least a factor of 16 [9]. Such irradiance levels can easily be achieved using simple light-emitting diodes instead of expensive laser illumination.

Experimental data reveal that the nonlinear current breakdown can be precisely adjusted by V_{bias} [cf. Figs. 5(a) and 5(b)], resulting in a change in the electric field across the intrinsic region, according to

$$E_i = \frac{V_{\mathrm{BI}} \pm V_{\mathrm{bias}}}{d_i}, \quad eV_{\mathrm{BI}} = E_M - E_{\mathrm{fp}} - E_{\mathrm{fn}}. \tag{3}$$

The built-in voltage V_{BI} arises from the energy of the mobility gap E_M and the Fermi energies within the doping areas that correspond to the band edges E_{fn} and E_{fp} [27]. At moderate reverse bias voltages, the intrinsic electric field E_i increases and effectively prevents field screening. As a result, the FIP is reduced or, in the case of highly negative V_{bias}, suppressed. Biasing the sensor near the sensor open-circuit voltage decreases the built-in field and increases screening to reinforce the FIP. The built-in field can also simply be tuned either by decreasing the *i*-layer thickness to reduce the FIP or by increasing the *i*-layer thickness to provide a more pronounced FIP as demonstrated in this paper and Eq. (3). Besides proper field engineering, it is possible to tune the current breakdown by forcing more charge carriers to be trapped by providing more defect states [cf. Eq. (2)]. The energetic position and the total density of states within the mobility gap can reliably be adjusted by the PECVD growth process of *a*-Si:H within a range of at least 10^{16} cm^{-3} [15] to 6×10^{19} cm^{-3} [28]. The most important origin of such defects, especially deep gap dangling bond states, is weak bond disorder in the atomic structure [29,30]. Such a weak bond disorder strongly depends on the growth conditions and can easily be adjusted by the deposition temperature, rf power [31], or the process pressure. The deposition mechanism has an impact not only on the atomistic bonding but also on the hydrogenation, the Urbach energy, and its temperature dependence [28]. Subsequent to the thin-film deposition, the weak bond distribution remains in its steady state, but

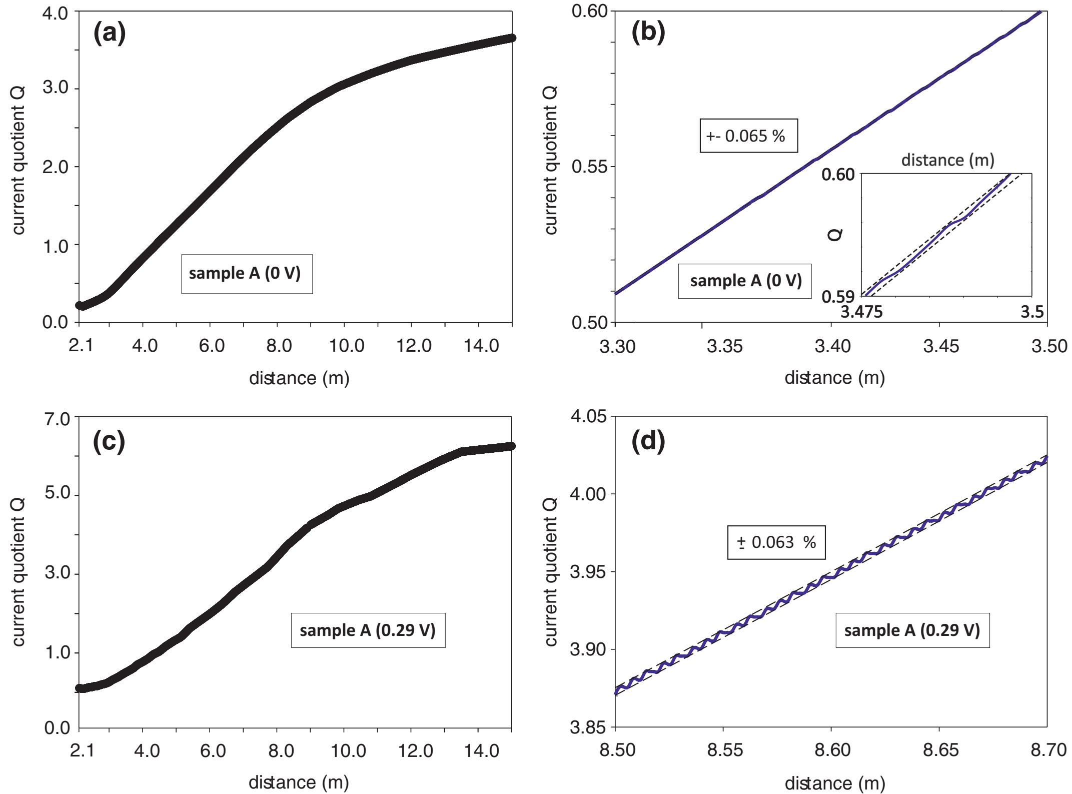

FIG. 6. (a) and (b) Current quotient Q of sample A as a measure of distance for 0 V and (c) and (d) 0.29 V at 488 nm. Distances of up to 15 m can clearly be distinguished. The relative derivation of Q for 3.3 m–3.5 m has been determined to be 0.065% corresponding to a depth resolution of $\Delta d = 2.1$ mm at 3.3 m. At 0.29 V, 0.063% can be achieved, resulting in $\Delta d = 5.5$ mm at 8.6 m.

can be modified reversibly by shifting the Fermi energy or by annealing [29,30,32].

C. dc distance measurements

The z-scan current measurements presented in Fig. 5 were employed to evaluate the performance (distance x, depth resolution Δd) for steady-state optical distance measurements exploiting the current breakdown near the focal plane. Therefore, a setup including a light source, a focusing lens, and two photodetectors at variable positions z_{s1} and z_{s2} was used to assess the distance-measurement capabilities of the device and to control precisely and reproducibly the optical power densities at the respective sensor positions (cf. Fig. S3 in the Supplemental Material [33]). Next, irradiances were matched to those obtained from the z-scan measurements listed in Fig. 5. Finally, the respective z-scan current was assigned to the distance-measurement setup, resulting in a detector current $I = f(x, z_s)$. Further information about the procedures, including a schematic of the modeled setup, are given in detail in the Supplemental Material [33]. Following the established routine [9], we determine a quotient Q of the detector currents I_1 and I_2 at two different sensor positions z_{s1} and z_{s2} to determine x and to eliminate the influence of the total light power:

$$Q = \frac{I_2(x, z_{s2})}{I_1(x, z_{s1})}. \qquad (4)$$

This measured quotient acts firstly to generate a calibration reference of the nonlinear system (which is necessary given the complex distance behavior of the nonlinearity) and secondly to measure distances, prior using such calibration values as a look-up table.

A first series recording of Q for sample A at 0 V bias allows distances up to at least 15 m [cf. Fig. 6(a)] to be measured. A second-degree polynomial quotient fit has been used to determine the achievable depth resolution Δd at a specific distance corresponding to the maximum relative difference to Q. Here, the relative difference to Q is 0.065% corresponding to $\Delta d = 2.1$ mm at a distance of 3.4 m [cf. Fig. 6(b)]. Simple tuning of the bias voltage to 0.29 V allows precise distance determination at larger distances for the same FIP sensor. The relative difference of Q for 0.29 V of 0.063% at 8.6 m results in an achievable depth resolution of $\Delta d = 5.5$ mm [cf. Fig. 6(d)].

The more pronounced bias tunability of the FIP in sample B enables an enhanced application-specific measurement flexibility. Applying different bias voltages, here

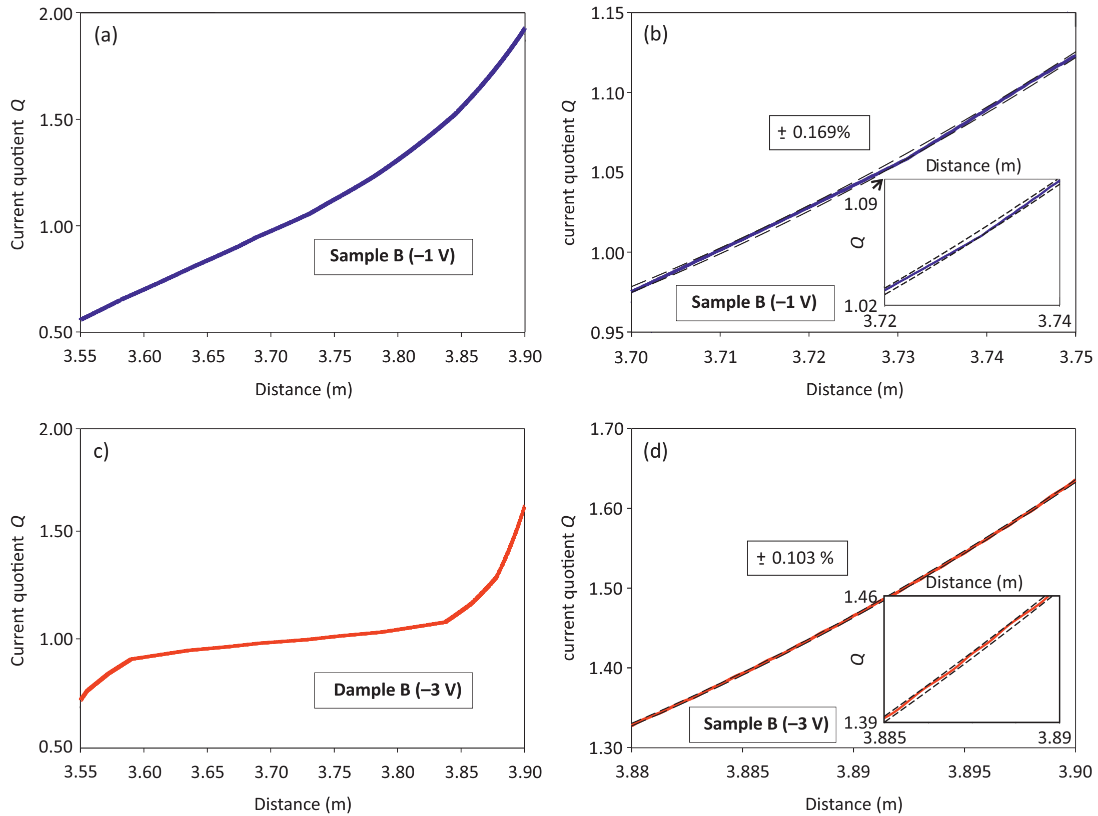

FIG. 7. (a) and (b) Current quotient Q of sample B as a measure of distance for −1 V and (c) and (d) −3 V at 488 nm. Since the achievable depth resolution Δd is directly related to the derivation of Q, both, Δd and the measurement sensitivity that depends on the absolute value of Q can simply be tuned by the applied bias voltage.

shown for −1 V and −3 V, facilitates the opportunity either to increase the distance-measurement range with a comparatively high accuracy or to achieve a maximum depth resolution at a specific distance (cf. Fig. 7). At a bias of −1 V, the measurement bandwidth with an almost constant high accuracy of 0.169% ($\Delta d = 6.32$ mm) covers 3.55 m−3.90 m, whereas a bias of −3 V results in an increase of the derivation of Q, hence the achievable depth resolution, and a maximum of up to 0.103% ($\Delta d = 4$ mm) at a distance range of 3.88−3.90 m.

To further increase Δd, the difference of two quotients ΔQ at a given distance difference Δx must be maximized. For static sensor positions, Q at a distance x_0 is given by Eq. (4). Assuming a linear current slope at small Δx, Q at a distance $x_0 + \Delta x$ results in

$$Q = \frac{I_2(x_0) + (dI_2/dx) \cdot \Delta x}{I_1(x_0) + (dI_1/dx) \cdot \Delta x}. \tag{5}$$

The variation of Q for small Δx is

$$\begin{aligned}\Delta Q &= Q(x_0 + \Delta x) - Q(x_0)\\ &= \frac{I_2(x_0) + (dI_2/dx) \cdot \Delta x}{I_1(x_0) + (dI_1/dx) \cdot \Delta x} - \frac{I_2(x_0)}{I_1(x_0)},\end{aligned} \tag{6}$$

which can be rewritten as (cf. Supplemental Material [33])

$$\Delta Q = \frac{(dI_2/dx) - Q(x_0) \cdot (dI_1/dx)}{(I_1(x_0)/\Delta x) + (dI_1/dx)}. \tag{7}$$

Equation (7) reveals that the variation of Q, and thus the depth resolution Δd, depends on

(a) the detector current gradients $(dI_{1,2}/dx)$,
(b) the absolute detector current $I_1(x_0)$, and
(c) on $Q(x_0)$ and the distance difference Δx itself.

According to Eq. (7) we evidently identify the z-scan current gradients $(dI_{1,2}/dz)$ to be the key parameters in achieving high-depth resolutions to exploit the nonlinear FIP for three-dimensional imaging applications.

Our results demonstrate that systematic material, device, and electric field engineering, combined with the bias tunability of the FIP, allows precise adjustments of $(dI_{1,2}/dz)$ and $I_1(z_0)$, enabling both high accuracy and long-range distance measurements in a single-pixel FIP sensor.

IV. CONCLUSION

The bias and irradiance-dependent current breakdown in *a*-Si:H *p*-*i*-*n* photodiodes was investigated systematically by electro-optical simulations and z-scan measurements for two different sensor architectures. We identify an irradiance-dependent enhancement of the built-in field in the front of both detectors close to the *p*-*i* interface due to irradiance-dependent locally occupied trapping states. The field deformation limits the charge carrier transport at high irradiances, resulting in a massive nonlinear current breakdown. We demonstrate an evaluation of steady-state distance measurements up to 15 m and a measurement precision of 2.1 mm (0.063%) at 3.3 m, 488 nm, and 0 V bias voltage. At 488 nm and 0 V bias, *a*-Si:H FIP sensors achieve a detection limit of at least 380 nW, corresponding to an irradiance of 0.6 μW/mm^2. We demonstrate that the bias-tunable FIP allows for both high-sensitivity and high-accuracy distance measurements at a specific distance. Simulations and experiments show that systematic and proper device and field engineering allow the sensor response to be precisely tailored for highly precise and/or long-range distance measurements. Since the versatile and mature low-temperature PECVD technology device fabrication is reproducible, scalable, and allows for sensor integration on top of silicon or flexible electronics with fill factors close to 100%, it provides the basis for further improving the performance of existing three-dimensional imaging systems.

ACKNOWLEDGMENTS

The authors are grateful to the European Regional Development Funds in North Rhine-Westphalia (EFRE.NRW) for funding this research project (EFRE0200545). Part of this work was performed at the DFG-funded Micro- and Nanoanalytics Facility (MNaF) of the University of Siegen (INST 221/131-1) utilizing its major ESEM instrument. In particular, we thank Dr. Yilmaz Sakalli for the operation of the tool. Moreover, we thank Marco Hepp and Dr.-Ing Julian Müller from the Institute of Micro- and Nanoanalytics of the University of Siegen for support in carrying out the ESEM analyses and three-dimensional visualization.

[1] R. H. Rasshofer and K. Gresser, Automotive radar and lidar systems for next generation driver assistance functions, Adv. Radio Sci. **3**, 205 (2005).

[2] S. Zhang, *Handbook of 3D Machine Vision: Optical Metrology and Imaging* (CRC Press, Boca Raton, FL, USA, 2013).

[3] A. Kolb, E. Barth, R. Koch, and R. Larsen, Time-of-Flight cameras in computer graphics, Comput. Graph. Forum **29**, 141 (2010).

[4] W. J. Tam, F. Speranza, S. Yano, K. Shimono, and H. Ono, Stereoscopic 3D-TV: Visual comfort, IEEE Trans. Broadcast. **57**, 335 (2011).

[5] R. Schwarte, Z. Xu, H.-G. Heinol, J. Olk, R. Klein, B. Buxbaum, H. Fischer, and J. Schulte, *Sensors, Sensor Systems, and Sensor Data Processing* (International Society for Optics and Photonics, 1997), Vol. 3100, pp. 245–253.

[6] P. Kienitz, A. Bablich, R. Bornemann, and P. H. Bolívar, *2D Photonic Materials and Devices IV* (International Society for Optics and Photonics, San Francisco, CA, USA, 2021), Vol. 11688, pp. 116880S.

[7] B. Behroozpour, P. A. M. Sandborn, M. C. Wu, and B. E. Boser, Lidar system architectures and circuits, IEEE Commun. Mag. **55**, 135 (2017).

[8] S. Soatto, R. Frezza, and P. Perona, Motion estimation via dynamic vision, IEEE Trans. Automat. Control **41**, 393 (1996).

[9] O. Pekkola, C. Lungenschmied, P. Fejes, A. Handreck, W. Hermes, S. Irle, C. Lennartz, C. Schildknecht, P. Schillen, P. Schindler, R. Send, S. Valouch, E. Thiel, and I. Bruder, Focus-induced photoresponse: A novel way to measure distances with photodetectors, Sci. Rep. **8**, 9208 (2018).

[10] E. Kasparavicius, S. Nakamichi, M. Daskeviciene, M. Marcinskas, L. M. Svirskaite, C. Lungenschmied, T. Malinauskas, V. Getautis, and I. Bruder, Focus-induced photoresponse technique-based NIR photodetectors containing dimeric polymethine dyes, J. Electron. Mater. **48**, 5843 (2019).

[11] Y. Wang, J. Benduhn, L. Baisinger, C. Lungenschmied, K. Leo, and D. Spoltore, Optical distance measurement based on induced nonlinear photoresponse of high-performance organic near-infrared photodetectors, ACS Appl. Mater. Interfaces **13**, 23239 (2021).

[12] V. L. Dalal and A. Rothwarf, Comment on "A simple measurement of absolute solar cell efficiency", J. Appl. Phys. **50**, 2980 (1979).

[13] S. S. Hegedus and W. N. Shafarman, Thin-film solar cells: Device measurements and analysis, Prog. Photovolt. **12**, 155 (2004).

[14] T. Lule, B. Schneider, and M. Bohm, Design and fabrication of a high-dynamic-range image sensor in TFA technology, IEEE J. Solid-State Circuits **34**, 704 (1999).

[15] G. Ganguly and A. Matsuda, Defect formation during growth of hydrogenated amorphous silicon, Phys. Rev. B **47**, 3661 (1993).

[16] D. L. Staebler, R. S. Crandall, and R. Williams, Stability of n-i-p amorphous silicon solar cells, Appl. Phys. Lett. **39**, 733 (1981).

[17] M. Lohrasbi, P. Pattanapanishsawat, M. Isenberg, and S. Chuang, *Degradation Study of Dye-Sensitized Solar Cells by Electrochemical Impedance and FTIR Spectroscopy* (IEEE, Cleveland, OH, USA, 2013), pp. 1–4.

[18] R. Varache, C. Leendertz, M. E. Gueunier-Farret, J. Haschke, D. Muñoz, and L. Korte, Investigation of selective junctions using a newly developed tunnel current model for solar cell applications, Sol. Energy Mater. Sol. Cells **141**, 14 (2015).

[19] A. Bablich, C. Merfort, H. Schäfer-Eberwein, P. Haring-Bolivar, and M. Boehm, 2-In-1 red-/green-/blue sensitive a-SiC:H/a-Si:H/a-SiGeC:H thin film photo detector with an integrated optical filter, Thin Solid Films **552**, 212 (2014).

[20] M. Sheik-Bahae, A. A. Said, T.-H. Wei, D. J. Hagan, and E. W. Van Stryland, Sensitive measurement of optical nonlinearities using a single beam, IEEE J. Quantum Electron. **26**, 760 (1990).

[21] K. Ikeda, Y. Shen, and Y. Fainman, Enhanced optical nonlinearity in amorphous silicon and Its application to waveguide devices, Opt. Express **15**, 17761 (2007).

[22] I. Sakata and Y. Hayashi, Theoretical analysis of trapping and recombination of photogenerated carriers in amorphous silicon solar cells, Appl. Phys. A **37**, 153 (1985).

[23] J. G. Shaw and M. Hack, An analytic model for calculating trapped charge in amorphous silicon, J. Appl. Phys. **64**, 4562 (1988).

[24] R. S. Crandall, Modeling of thin film solar cells: Uniform field approximation, J. Appl. Phys. **54**, 7176 (1983).

[25] M. Hack and M. Shur, Physics of amorphous silicon alloy p-i-n solar cells, J. Appl. Phys. **58**, 997 (1985).

[26] K. Misiakos and F. A. Lindholm, Analytical and numerical modeling of amorphous silicon p-i-n solar cells, J. Appl. Phys. **64**, 383 (1988).

[27] R. A. Street, *Hydrogenated Amorphous Silicon*, 1st ed. (Cambridge University Press, Cambridge, 1991).

[28] J. Robertson, Deposition mechanism of hydrogenated amorphous silicon, J. Appl. Phys. **87**, 2608 (2000).

[29] R. A. Street and K. Winer, Defect equilibria in undoped A-Si:H, Phys. Rev. B **40**, 6236 (1989).

[30] K. Winer, Chemical-Equilibrium Description of the Gap-State Distribution in a-Si:H, Phys. Rev. Lett. **63**, 1487 (1989).

[31] J. C. Knights and G. Lucovsky, Hydrogen in amorphous semiconductors, Crit. Rev. Solid State Mater. Sci. **9**, 211 (1980).

[32] M. J. Powell and S. C. Deane, Improved defect-pool model for charged defects in amorphous silicon, Phys. Rev. B **48**, 10815 (1993).

[33] See Supplemental Material at http://link.aps.org/supplemental/10.1103/PhysRevApplied.17.034075 for in-depth information on the simulation routine, device fabrication and fundamental characterization and the distance measurement.